Article

Surfactant-Free Synthesis of Melon Seed−Like CeO$_2$ and Ho@CeO$_2$ Nanostructures with Enriched Oxygen Vacancies: Characterization and Their Enhanced Antibacterial Properties

Kanwal Javed, Yufang Ren, Zhenhao Cao, Bushra Begum, Yifan Liu, Aamad Ullah Zafar, and Xue Li*

Read Online

ACCESS | Metrics & More | Article Recommendations | SI Supporting Information

ABSTRACT: To overcome the poor antibacterial performance of cerium oxide (CeO$_2$) nanoparticles at low concentrations, melon seed−shaped CeO$_2$ (MS-CeO$_2$) and holmium (Ho)-doped CeO$_2$ (Ho@MS-CeO$_2$) nanoparticles were synthesized using a simple precipitation method without the addition of any surfactants. The surface morphology, phase structure, crystallinity, Ce^{3+} and Ce^{4+} valence, lattice defects, and reactive oxygen species (ROS) production of both synthesized nanostructures were examined using different techniques, i.e., scanning electron microscopy (SEM), energydispersive X-ray (EDX), resolution transmission electron microscopy (TEM), high-resolution transmission electron microscopy (HRTEM), Fourier transform infrared spectroscopy (FT-IR), X-ray diffractometry (XRD), X-ray photoelectron spectroscopy (XPS), electron paramagnetic resonance (EPR), Raman spectroscopy, ultraviolet (UV)

spectra, fluorescence spectra, and zeta potential (ζ). The results show that under certain stirring and aging temperatures, CeO$_2$ and Ho-doped CeO$_2$ nanoparticles with a melon seed−like morphology can be prepared in a short period. Both nanoparticles were tested as antiseptic agents against G$^+$ and G$^−$ bacteria (E. coli and S. aureus), and the results confirmed that the Ho@MS-CeO$_2$ nanostructures exhibited remarkable antimicrobial activity at a low concentration (0.5 mg/L) compared with the control group, which is attributed to the reversible conversion of Ce^{3+} and Ce^{4+} in the ceria crystal lattice, enriched oxygen vacancy, ROS species production, and positive surface charge.
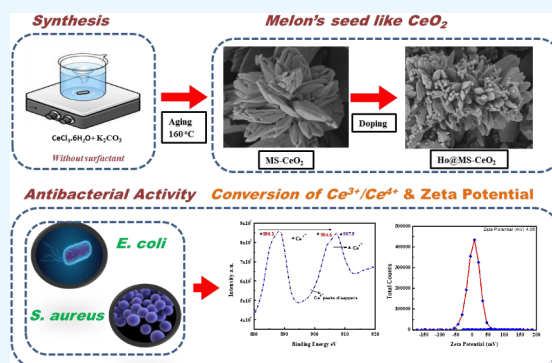
1. INTRODUCTION

Cerium oxide (CeO$_2$) has a cubic fluorite structure that can give cations with two different oxidation states (i.e., Ce^{3+} and Ce^{4+}).[1] The Ce^{4+} cation is bounded by eight O$^{2−}$ ions. Reportedly, due to the oxygen vacancies (O$_v$), the Ce coordination number is reduced to seven, and the oxygen atom (O$_{atm}$) leaves two additional electrons while accompanied by Ce^{3+}, which affected the length of the Ce−O bond and lattice constant. Therefore, the amount of Ce^{3+} may be considered an active parameter for the formation of oxygen vacancies.[2,3] Thus, the vacancies can be truly ascribed to the oxygen atom.[3] The capability of CeO$_2$ to convert between dual oxidation (+3 and +4) states permits the storage capacity as well as the discharge of oxygen, high thermal stability, precise chemical reactivity, hardness, and electrical conductivity.[1] Its redox action and the oxygen vacancies caused by surface defects endow it with different biological activities, such as antiapoptotic, anti-inflammation, and antioxidant properties.[4,5] Therefore, in recent years, the synthesis of CeO$_2$ nanomaterials with unique properties has attracted much attention.[4]

Compared with other metal oxides, CeO$_2$ is a promising material and functions as an excellent antibacterial agent with low toxicity in medical and biological fields.[6,7] It has also been found that CeO$_2$ has remarkable antibacterial properties against many bacteria, mainly due to the production of reactive oxygen species (ROS),[7,8] or is attributable to electrostatic interaction,[8] which attracts CeO$_2$ nanoparticles to the cell membrane of bacteria, resulting in protein denaturation, membrane impermeability, and finally, bacterial death.[7] However, many researchers have found that CeO$_2$ cannot damage bacterial biofilms at very low concentrations (1−5 mg/L),[6] indicating unsatisfactory antibacterial effects. To improve the antibacterial performance of CeO$_2$ nanomaterials and expand their application range, some investigations have been done on doping CeO$_2$ structures with different types of dopant elements.[6,8] For example, Balamurugan et al.[9] doped CeO$_2$ nanoparticles with Sm dopants, which exhibited enhanced antibacterial activity against infective bacteria. Negi et al.[10] synthesized Ag/CeO$_2$ nanomaterials, which displayed
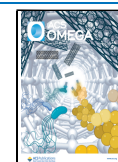
improved antibacterial property toward *S. aureus* and *P. aeruginosa* bacteria. Some researchers also doped gadolinium, europium, and cadmium with CeO_2 nanoparticles, which showed better antimicrobial activity against pathogenic bacteria, such as *E. coli*, *S. aureus,* and *Bacillus cereus*.[5,8,11] Although there has been some research on the doping of CeO_2 nanoparticles, it is still necessary to find new doping systems to further improve their antibacterial properties, which is of great significance for the application of CeO_2 nanoparticles. In addition, the structure-dependent antibacterial performance and antibacterial mechanism of doped CeO_2 nanoparticles also need to be studied. Table S1 summarizes the latest research results on CeO_2 and doped CeO_2 nanoparticles with different shapes and structures, demonstrating their antibacterial performance against different bacterial strains.

CeO_2 nanomaterials can be prepared by different synthetic methods ,such as hydrothermal process, microemulsion, sol—gel precipitation, spray pyrolysis, solvothermal synthesis, coprecipitation.[2,12] Previous reports have shown that the CeO_2 nanoparticles (NPs) can easily be synthesized through the coprecipitating method by using $Ce(NO_3)_3 \cdot 6H_2O$ with poly(vinylpyrrolidone) (PVP) or poly(ethylene glycol) (PEG) in a basic solution.[12] However, the large sizes of polydispersed and aggregated particles were also obtained under as a surfactant. But by using hexamethylenetetramine (HMT) surfactant, stable CeO_2 NPs with sizes in 2.6 to 240 nm ranges were obtained by increasing the reaction time.[12] Majumder et al.[2] synthesized flower-shaped CeO_2 by using a cerium ammonium nitrate precursor and PVP under ultrasonication. Sun et al.[13] fabricated polycrystalline CeO_2 nanowires with the shape-directing agent sodium bis (2-ethylhexyl) sulfo-succinate. However, research on CeO_2 nanomaterials with uniform morphologies that are selectively synthesized by the precipitation method without additives or surfactants is very scarce. Moreover, studying the effect of CeO_2 nanomaterials with improved oxygen vacancies on their antimicrobial properties is still a great challenge.

In this work, surfactant-free synthesis of uniform melon seed—shaped CeO_2 (MS-CeO_2) and Ho@MS-CeO_2 nanostructures with enriched oxygen vacancies was reported by a simple precipitation route. The structures and morphologies of the as-prepared nanoparticles were studied by SEM, EDX, TEM, HRTEM, FTIR, XRD, and XPS. The morphological effects of MS-CeO_2 as well as Ho@MS-CeO_2 nanostructures on their antibacterial activities were also investigated. Compared with the previously reported work, the MS-CeO_2 and Ho@MS-CeO_2 nanostructures exhibited a much better antibacterial efficiency. To the best of our knowledge, no previous studies have been reported on the Ho-doped CeO_2 nanoparticles and their antibacterial properties at low concentrations. The synthesis route reported here has the characteristics of low cost and simple preparation. The generated MS-CeO_2 and Ho@MS-CeO_2 nanoparticles may have great potential for different applications, such as in biomedical and food storage industries, due to their reversible conversion of ions, biocompatibility, and unique morphology with enhanced oxygen vacancies.[14−17]

2. EXPERIMENTAL SECTION

2.1. Materials. Ce (III) chloride ($CeCl_3 \cdot 7H_2O$) and potassium carbonate (K_2CO_3) were obtained from Macklin alongside Sinopharm Chemical Material Co. and utilized as received. Bactericides strains ,i.e., *Escherichia coli*(*E. coli*) (ATCC 25 922) and *Staphylococcus aureus* (*S. aureus*) (ATCC 6538) were assimilated from the Luwei Company, while sodium chloride (NaCl), nutrient agar Luria−Bertani (LB), and broth were acquired from Solarbio. For doping of CeO_2, holmium nitrate ($Ho(NO_3)_3 \cdot 5H_2O$) was purchased from the Macklin Company.

2.2. Synthesis of MS-CeO_2 and Ho@MS-CeO_2 Nanoparticles. Melon seed-like CeO_2 nanoparticles were synthesized by a precipitation method. A 0.02 M aqueous solution of $CeCl_3 \cdot 7H_2O$ and 0.03 M aqueous solution of K_2CO_3 were separately prepared. Then, specific amount of $CeCl_3 \cdot 7H_2O$ and K_2CO_3 solutions were mixed dropwise in a beaker under constant stirring. Afterward, white precipitates started to appear. Subsequently, after 30 min of stirring, the resulting particles were collected and aged at 160 °C for 1 h. Then, the reactor was cooled and the resulting white particles were washed and dried at 100 °C for 4 h and cooled to room temperature. During the doping process, a holmium nitrate ($Ho(NO_3)_3 \cdot 5H_2O$) solution of 0.05 M concentration was added to the above experimental mixture and constantly stirred for 30 min and vice versa-

2.3. Characterization. The morphologies of pure and doped MS-CeO_2 nanoparticles were evaluated by scanning electron microscopy (SEM., JEOL). For this analysis, the selected particle samples of were placed on aluminum stubs using a double-sided tape (carbon conducting). Stubs were sputtering for 30 s using a fine coater (JEOL) with a uniform layer of platinum while maintaining a distance of about 10 mm between the tip of the gun and the holder of the sample at a rate of 15 kV. The existence of different functional groups on the surgace of the material and the intensity of their stretching bands were evaluated using a Fourier transform infrared spectrometer (FTIR 8400). The FTIR dimensions and stretching bands were accomplished in the mid-infrared region, i.e., 4000−400 cm^{-1} with a 4 cm^{-1} resolution in the spectrum. For this, a small quantity of sample was grounded and mixed with an appropriate amount of potassium bromide (KBr), transferred to a cup, and placed in a separate reflectance accessory for analysis. The structures and crystallite sizes were further assessed by the X-ray diffraction (XRD) method. Measurements were carried out through a diffractometer (JEOL JDX-3532) with Cu Kα wave radiation (λ = 0.1542 Å). The 2θ angle was approximately 10−80° range with a scan speed of about 0.05°2θ/s, while the steep position was at 0.1°/s for the sample. The CMPR and JDX-3500 softwares were used to analyze the peaks and crystalline phases for the test samples. Diameter, size, and shape distribution of the particles were studied by transmission electron microscopy (TEM JEM-1400) imaging with a line resolution of 0.2 mm and point resolution of 0.38 nm. TEM samples were made by spreading the small powder in ethanol under ultrasonication for 20 min, while HRTEM determined the crystallinity at the atomic level of the particle. HRTEM study was done on the JEM-2100F TEM instrument of JEOL (Nippon Electronics Co., Lt), which was operated at an accelerating voltage of about 120 kV. Energy-dispersive X-ray analysis (EDX) was used to determine the composition of elements of specific nanomaterials (JEOL Gemini 300, Germany). The components on the surface of the material andits electronic structure were inspected by X-ray photoelectron spectroscopy (XPS). It is used by means of a thermo K-α spectrometer mounted with monochromatic Al−Kα radiation.

2.4. Antibacterial Property. The antibacterial properties of MS-CeO$_2$ and Ho@MS-CeO$_2$ nanoparticles were studied using a standard precise agar disc diffusion technique. Typical cultures of *E. coli* and *S. aureus* strains were used and examined through the Kirby−Bauer method as follows: 100 μL of the bacterial solutions were taken and grown-up by adding 10 mL of LB broth in a shaking tube wrapped by using a brownish paper and placed in the shaker (120 rpm) at 37 °C for about 12 h.

Then, 8 mL of the above solutions was placed in a separate centrifuge tube and set in the centrifuge machine for 10 min (3000 rpm), and the supernatant was poured out after centrifugation. Again, 8 mL of NaCl solution was added to it and centrifuged for 10 min, the supernatant was decanted, and then 8 mL of NaCl was added to it and kept aside and named **A**. For measuring the optical density (OD) value (1.5 × 10^8 CFU/mL), 500−550 μL from bacterial solution **A** was taken in a separate tube and 5 mL of NaCl was added to it. 200 μL of solution was taken from it, and put into a 96-well plate through a pipette gun, and the concentration was 10^8 CFU/mL. Further conversion of 10^8 to 10^6 CFU/mL through the dilution method was obtained by taking 50 μL of the above bacterial mixture and adding 5 mL of LB liquid, which was named **B**. Then, 200 μL from bacterial solution **B** was taken in a separate centrifugation tube and mixed one by one with each sample of MS-CeO$_2$ (1 mL) and Ho@MS-CeO$_2$ nanostructure (1 mL) of various concentrations, i.e., 0.5, 1, and 2 mg/mL, wrapped in brown paper, and placed well in a shaker for 4 h (Liquid method) at 37 °C. During this time, we prepared nutrient-solid agar for every sample and poured molten agar (almost 20 mL) into a Petri dish and allowed to cool. 200 μL of each liquid sample (bacterial solution with CeO$_2$) was poured with a pipette gun into the Petri dishes (Muller agar plates) one by one, spread on the surface with the balls and dried so that no solvent remained. The discs were incubated for 24 h in an oven at 37 °C.

3. RESULTS AND DISCUSSION

3.1. Experimental Conditions. Experimental conditions, i.e., salt solutions, aging temperature, and time used in the preparation of MS-CeO$_2$ nanoparticles,significantly important influence their morphology. To obtain desirable uniform nanomaterials, the above-mentioned synthesis factors were systematically optimized without using any organic surfactant or template.

3.1.1. Morphology of MS-CeO$_2$ and Ho@MS-CeO$_2$ Nanoparticles. When the CeCl$_3$·7H$_2$O precursor (0.02 M) was mixed with 0.03 M K$_2$CO$_3$ precipitating agent at room temperature under stirring, white precipitates began to form. When the precipitates were heated at 160 °C, CeO$_2$ nuclei formation occurred. Based on Ostwald ripening route, the melon seed−like CeO$_2$ morphology originated in this system, as shown in Figure 1a−c.[18]

Many researchers synthesized ceria nanomaterials through different methods using various precipitating agents such as ammonium carbonate, and sodium hydrogen carbonate to obtain agglomerated[19] and larger-size particles.[16] Hapsari et al.[20] synthesized Gd-CeO$_2$ using potassium carbonate (K$_2$CO$_3$) and potassium hydroxide (KOH) as precipitants and evaluated the effects of K$_2$CO$_3$ on the morphology of CeO$_2$. It showed that the morphology of the nanosheets was changed when using K$_2$CO$_3$ as a precipitant. In this work, when K$_2$CO$_3$ was added in CeCl$_3$ aqueous solution under
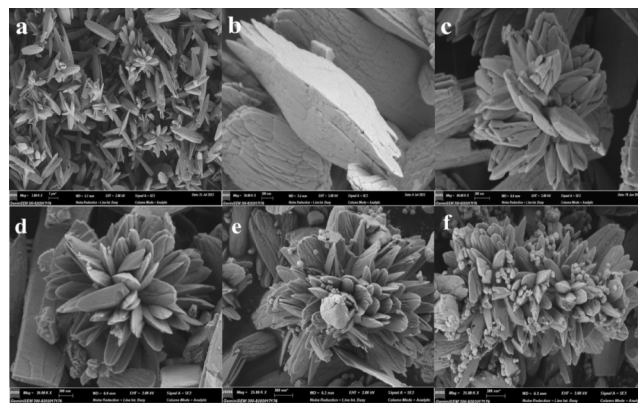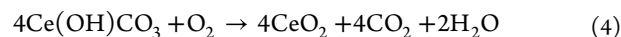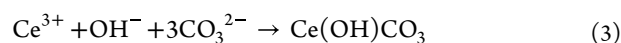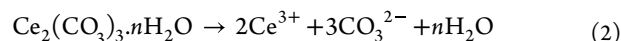

Figure 1. SEM images of MS-CeO$_2$ and Ho@MS-CeO$_2$ nanoparticles prepared by (0.02M) CeCl$_3$ and (0.03M) K$_2$CO$_3$ and aged at 160 °C for 1 h displayed at different magnifications. (a−c) MS-CeO$_2$ and (d−f) Ho@MS-CeO$_2$ while Ho content: (d) 1 wt %, (e) 2 wt %, and (f) 3 wt %.

stirring, Ce^{3+} ions reacted violently with CO$_3^{2-}$, and meanwhile, white precipitates were instantly generated. Additionally, when the precipitates countered with OH$^-$ and formed Ce^{3+} basic carbonates [Ce(OH)CO$_3$], they were self-accumulated, oxidized, and molded into MS-CeO$_2$ in an O$_2$-rich atmosphere, as shown in Figure 1c and reactions 1−4.[21]

$$K_2CO_3 \rightarrow K^+ + CO_3^2 \tag{1}$$

$$Ce_2(CO_3)_3 \cdot nH_2O \rightarrow 2Ce^{3+} + 3CO_3^{2-} + nH_2O \tag{2}$$

$$Ce^{3+} + OH^- + 3CO_3^{2-} \rightarrow Ce(OH)CO_3 \tag{3}$$

$$4Ce(OH)CO_3 + O_2 \rightarrow 4CeO_2 + 4CO_2 + 2H_2O \tag{4}$$

Similarly, Figure 1d−f shows the morphology of Ho@MS-CeO$_2$ at Ho concentrations of 1, 2, and 3 wt %. The results show that Ho doping did not affect the morphology of MS-CeO$_2$. It has been reported that the smaller ionic radii of heteroatom dopants (relative to pure CeO$_2$) can cause changes in the equilibrium lattice constant of doped nanomaterials, which in turn would lead to distortion of the local symmetry.[22,23] However, in this work, the dopant Ho in CeO$_2$ did not cause any distortion of symmetry due to its higher ionic radius. While strong diffraction points of doped MS-CeO$_2$ nanoparticles demonstrated their high crystalline nature.[22] The doping of Ho metal on CeO$_2$ might reduce the concentration of Ce^{4+} ions through increase in the concentration of Ce^{3+} ions (redox reactions), which is related to oxygen vacancies, and has played a dominant role in lattice distortion.[22] Figure 2 shows the EDX spectra of 3 wt % Ho@MS-CeO$_2$ nanoparticles. The presence of Ce, O, and Ho can be observed in the sample, where Ce and O elements spread everywhere and Ho existed in the same areas of the nanoparticles. Ce = 71.65% and O = 25.34% confirmed the presence of CeO$_2$, while the Ho metal content was almost 3.01%, as summarized in Table S1.

3.1.2. Effects of Reaction Time and Aging Time. The main outcome of the time factor is to simplify the synthesis process of nanomaterials in a shorter time, comprising, particularly, structural destabilization and Ostwald ripening.[24] In this work, when the reaction time was less than 10 min, no turbidity was observed in the solution mixture. Onward from 10 to 20 min, a translucent colloidal solution began to form, indicateing the
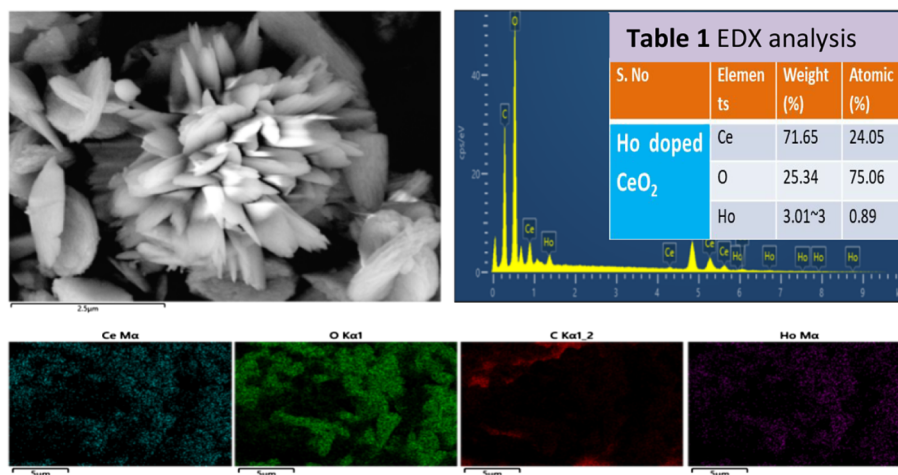
Figure 2. EDX spectra and elemental mapping analysis of Ho@MS-CeO$_2$ nanoparticles. The content of Ho is 3 wt %.

formation of nanoparticles. When the reaction time increased further, a white colloidal solution was observed at 20 to 40 min, with constant stirring at room temperature (Figure S1). These observations showed that the aggregation and particle size of ceria nanocrystals progressively increased together with increased stirring time.[24]

Figure 3 shows the SEM images of MS-CeO$_2$ nanoparticles at different times. At the initial time (10 min), the particles still
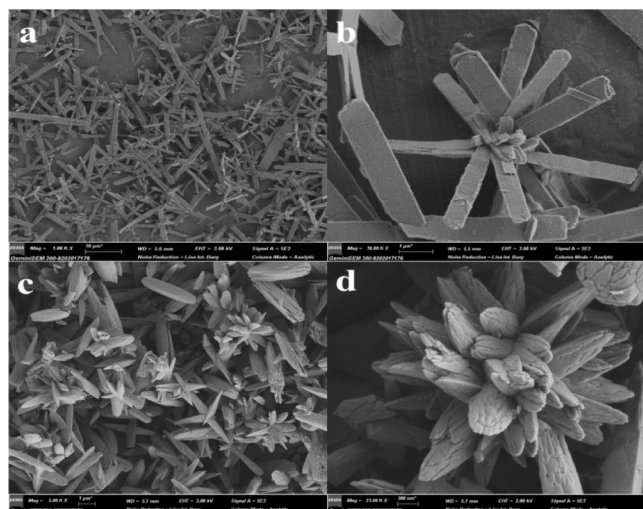

Figure 3. SEM images of MS-CeO$_2$ nanoparticles at different aging times: (a) 10, (b) 30, (c) 40, and (d) 60 min.
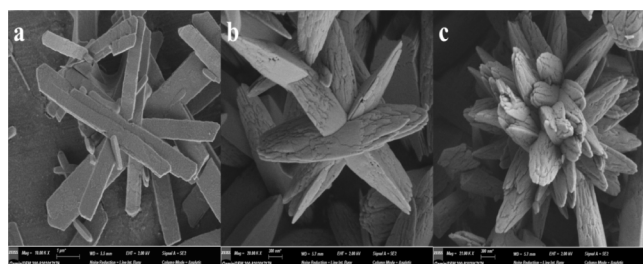

Figure 4. Effect of temperature on the morphology of CeO$_2$ (i.e., (a) at room temperature, (b) 120 °C, and (c) 160 °C.

had sheet-like morphology (Figure 3a,b) similar to Figure 4a during stirring at room temperature. Upon aging for 30 min, the morphology of the particles did not change. While aging for more than 40 min, the melon seed morphology of CeO$_2$ formed (Figure 3c,d), illustrating that both reaction and aging time factors are important for the preparation of nanoparticles with the desired morphology. Sakthivel et al.[25] investigated the effect of aging time on the growth rate of ceria nanoparticles. The growth rate fluctuated with time and reached to its maximum size range after 24 h and then started to decrease in size over time.[25] Zhang et al.[26] synthesized several uniform [Ce(OH)CO$_3$] flowers from a reaction of Ce(NH$_4$)(NO$_3$)$_4$ with CO(NH$_2$)$_2$ by using water-N$_2$H$_4$ complex at 160 °C for 24 h. After thermal conversion at 500 °C for almost 6 h, they obtained CeO$_2$ flowers. They studied the effect of reaction time and concluded that uniform dendrites were obtained in a longer time (15−18 h), and then, symmetric flowers were obtained at 21 h. In the present work, the determined reaction time was only 30 min, while the aging time was just 1 h for the fully suitable growth of MS-CeO$_2$ nanoparticles (Figure 3d). Synthesis of desirable CeO$_2$ nanostructures is very difficult to attain without any surfactant or complex within 1 h of aging time. However, this work signified uniformity during the synthesis of every single crystal without any surfactant to form MS-CeO$_2$ nanoparticles.

3.1.3. Effect of Temperature. Temperature is another factor that has a great impact on the feature of CeO$_2$ nanomaterials. Before aging, all particles first exhibited a sheet-like morphology at room temperature (Figure 4a). When aged at 120 °C, the particles grew thicker and changed their features, reflecting an effect of temperature on the CeO$_2$ crystallization procedure (Figure 4b). Since high temperature causes a faster nucleation,[27] therefore, when the aging temperature increases to 160 °C, many melon seed−like CeO$_2$ nanoparticles are formed (Figure 4c). At room or lower temperatures, nano-octahedral particles form because of their less stable structure and lack of sufficient energy to overcome the surface energy.[28]

When the temperature increases, the morphology of nanoparticles changes due to Gibbs free energy, which easily overcomes the surface energy; thus, the growth process begins, and different shape nanoparticles are found. The process of heat treatment provided sufficient energy for nucleation, enhancing the surface mobility. It also increased the collision frequency among nucleating atoms that dispersed during the

synthesis process, which made the surface more active, diminishing the creation of constricted aggregates.[29] The consequence of this process is the formation of crystalline nanoparticles with melon seed−like morphology.[27]

Under normal circumstances, different morphologies might also be attained at the same temperature[22] because they totally depend on synthesis conditions, i.e., reaction time and initial composition of the solution. Wu et al.[30] studied the influence of counteranions of cerium source on the shape of the generated nanoparticles and found that nanoparticles with different morphologies could be formed at the same temperature. In our method, a distinctive combination of chloride and carbonate ions is used to generate crystalline and stable MS-CeO_2 nanoparticles at specific synthesis temperatures without any template.

3.2. Structure of MS-CeO_2 and Ho@MS-CeO_2 Nanoparticles.

The crystal structure of MS-CeO_2 and Ho@MS-CeO_2 nanoparticles were observed by TEM and HRTEM. The TEM images revealed that the single melon seed−like crystal joined together to form a distinct morphology (Figure 5a,b),
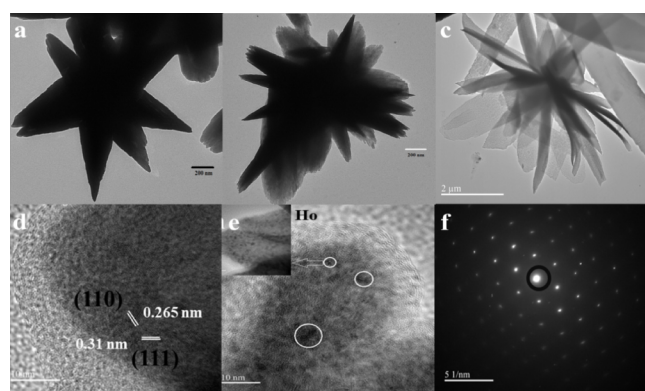

Figure 5. TEM images of (a) pure MS-CeO_2 and (b) Ho@MS-CeO_2. HRTEM images of (c) pure MS-CeO_2, (d,e) Ho@MS-CeO_2, and (f) SAED pattern of Ho@MS-CeO_2.

which is consistent with the SEM observations (Figure 1c,f). Figure 5c is an HRTEM image of pure MS-CeO_2, which displays a clear MS morphology, while Figure 5(d) of Ho@MS-CeO_2 has clear lattice fringes and the plane distance, i.e.,

0.265 and 0.31 nm, consistent with the d-spacing values of (110) and (111) planes of the FCC phase of CeO_2.[31,32] It has been reported that (110) plane exhibits greater oxygen vacancies than (111) for the CeO_2 plane.[1] Therefore, more oxygen vacancies and their transportation will happen in the nanocrystal and the redox reactions may occur on the CeO_2 surface for biological activities.[1] Figure 5e displays clearly many dark spots under the circle of the doped metal (Ho) on MS-CeO_2, while SAED image (Figure 5f) shows several electron diffraction spots in the regular pattern of MS-CeO_2. On the contrary, irrespective of the several diffraction spots, one asymmetrical size spot was found in a steady pattern, which confirmed the insertion of dopant metal on the surface of the ceria.

The crystal structures and phase purity of the synthesized pure MS-CeO_2 and Ho@MS-CeO_2 were further assessed by XRD technique (Figure 6A). It was observed that all diffraction peaks were assigned to the FCC phase of CeO_2, while no other extra diffraction peaks were detected suggesting the purity of CeO_2.[33,34] Here, in Figure 6A (spectrum a), the diffraction peaks at 2θ, 20.6, 26.5, 28.5, 33.08, 47.47, 38.1, 42.0, and 62.5°, were observed, which corresponded to the (110), (112), (111), (200), (220), (104), (213), and (404) planes of CeO_2 (JCPDS file 00−044−1001).[33,35] Figure 6A (spectrum b) shows the diffraction peaks of 3% Ho@MS-CeO_2 and their small shifting due to the increase in lattice defects, demonstrating that Ho^{3+} was successfully introduced as a dopant in MS-CeO_2 crystal.[36] However, due to the amorphous nature of the lanthanide oxides, the doping process did not introduce any secondary phase and Ho@MS-CeO_2 nanostructure remained the intrinsic crystal lattice of ceria.[37] Moreover, no diffraction peaks of Ho_2O_3 were observed, which implied that Ho^{3+} was ideally introduced into pure CeO_2.[38,39]

The average crystallite size of MS-CeO_2 nanostructure (Figure 6A (spectrum a)) was calculated using the Scherer equation from XRD data, which was specifically based on broadening of the peaks as well as the Bragg angle, which was approximately 13.1 nm, as summarized in Table S2. Figure 6A (spectrum b) shows the increase in the full width at half-maximum (fwhm) value for all the peaks of Ho@MS-CeO_2 and indicated the crystallite size decreases (~11.7 nm).[40] The reduction in the crystallite size was ascribed to the formation of
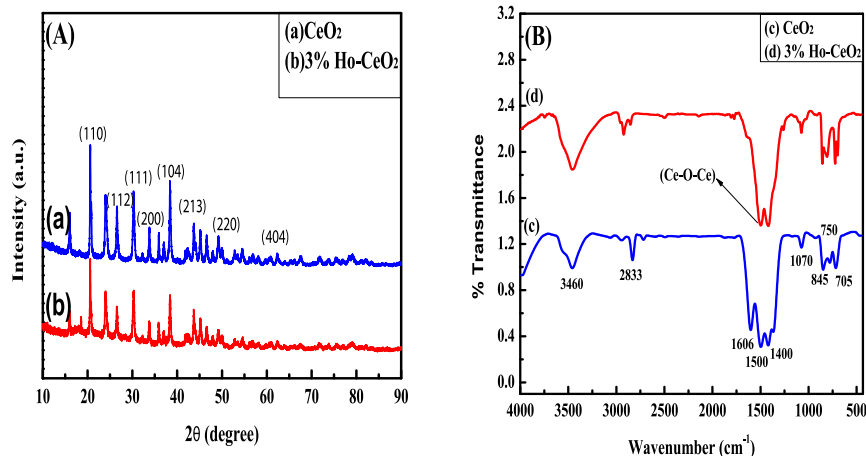

Figure 6. [A] XRD spectra of pure MS-CeO_2 (spectrum a) and Ho@MS-CeO_2 (spectrum b); [B] FTIR spectra of pure MS-CeO_2 (spectrum c) and Ho@MS-CeO_2 (spectrum d).
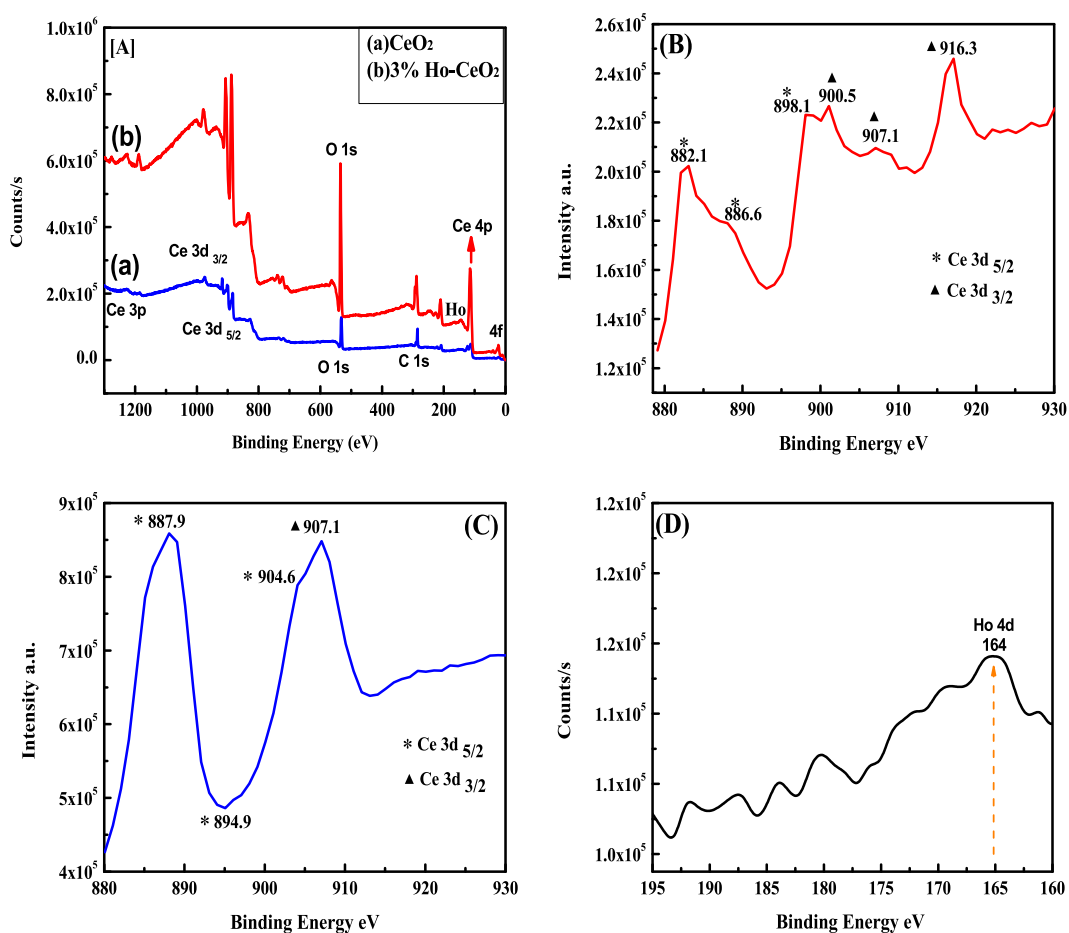
Figure 7. XPS spectra of (A) (a) pure MS-CeO$_2$ and (b) Ho@MS-CeO$_2$; (B) high-resolution XPS spectrum of Ce 3d for MS-CeO$_2$,;(C) high-resolution XPS spectrum of Ce 3d for Ho@MS-CeO$_2$; and (D) Ho^{3+} peaks in MS-CeO$_2$ nanostructure.
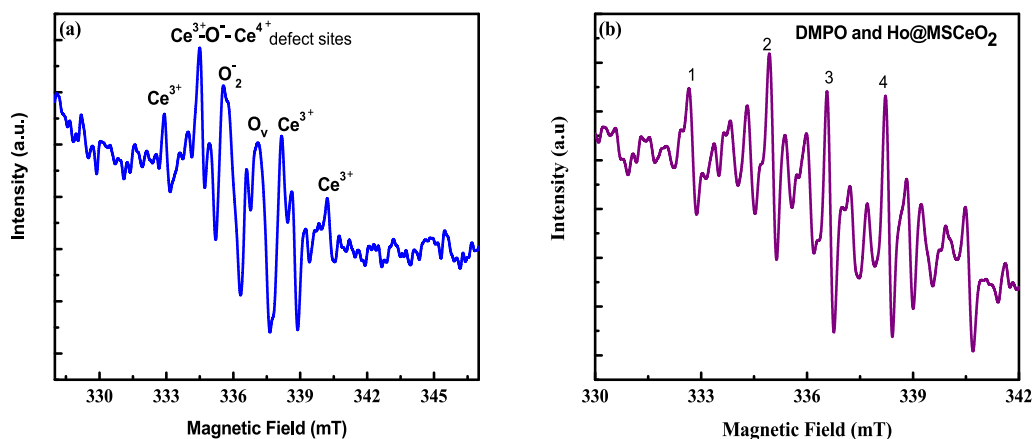

Figure 8. (a) EPR profile measured for MS-CeO$_2$ in methanol and (b) DMPO spin-trapping ESR profile for Ho@MSCeO$_2$.

Ho−O−Ce on the surface of crystal, which efficiently inhibited the growth of CeO$_2$ crystal grains.[40,41]

3.3. Chemical Composition of MS-CeO$_2$ and Ho@MS-CeO$_2$. The FTIR spectra of MS-CeO$_2$ and Ho@MS-CeO$_2$ are shown in Figure 6B. The adsorption peaks were 705, 750, 845, 1070, 1400, 1500, 1606, 2833, and 3460 cm^{-1}. The peak at 705 cm^{-1} or below range was ascribed to the Ce−O stretching and confirmed the formation of the CeO$_2$ structure.[4,42] The peaks at 750 and 1500 cm^{-1} describe the bonds of Ce−O stretching and Ce−O−Ce stretching vibrations, respectively.[43]

The 845 cm^{-1} peak is due to the absorption of the C−O−C stretching frequency. The absorption peak at around 3460 cm^{-1} is for O−H stretching vibrations. The peak intensities of Ce−O−Ce stretching vibrations for the Ho@MS-CeO$_2$ sample (Figure 6B (spectrum d)) decreased compared with those for the pure MS-CeO$_2$ (Figure 6B (spectrum c)), which clearly suggested the oxygen vacancies and mobility in CeO$_2$ were boosted through doping of Ho^{3+} ions.[43] The other remaining peaks are summarized in Table S3.

XPS was performed to complete the study of the chemical composition of the synthesized doped and undoped MS-CeO$_2$, as shown in Figure 7A.[44] The Ce 3d spectrum displays six peaks, which allotted to the 3d$_{5/2}$ state as well as peaks indexed to the 3d$_{3/2}$ state of Ce (IV)[45] (Table S4). Figures 7B,C displays the high-resolution spectrum of Ce 3d for MS-CeO$_2$ and Ho@MS-CeO$_2$. Figure 7D shows a broader view of 4d Ho^{3+} peaks in the MS-CeO$_2$ nanostructure.[46,47] A previous study specified that the electrons that occupied the new gap states were precisely localized on Ce cations adjacent to the oxygen vacancies, resulting in the reduction of two Ce^{4+} into Ce^{3+}. Meanwhile, O vacancies are related to the formation of Ce^{3+}; therefore, they are an indicative of the promising formation of Ce^{3+} with O vacancy in CeO$_2$.[37] It could be suggested that lanthanide elements (Ho) facilitate the formation of O vacancies in CeO$_2$ and reduce Ce^{4+} into Ce^{3+}. Hence, the concentration of Ce^{3+} increased significantly with a high intensity of oxygen vacancies (Figure 7A(b)), while displayed the clearest growth (O peak) with Ho-CeO$_2$.[37] The high content of Ce^{3+} led to huge lattice strain and consequent lattice constant expansion due to the differences in the size of the crystal radius (Ce^{3+} > Ce^{4+}). Therefore, the lattice expanded after doping and increased the O vacancies in nanomaterials.[37] Similarly, the size reduction of the CeO$_2$ nanoparticles released additional oxygen, causing O vacancies on their surfaces as well as the crystal defects.[48] Moreover, the smaller Ce 4f peak in Figure 7A also presented that the sample must contain Ce^{3+} ions in it.[49] The energy band peak at 532.2 eV was attributed to oxygen vacancies.[49]

Furthermore, the presence of lattice defects and oxygen vacancies in the nanostructures was confirmed by EPR characterization (Figure 8). In general, the existence of oxygen vacancies or defects in CeO$_2$ crystals is prompted by the loss of oxygen. To stabilize the defects, the Ce^{4+} converted into Ce^{3+},[48] which increases the Ce^{3+} level and redox potential on the surface of nanoceria, thereby enhancing antibacterial activity.[50] As follows, MS-CeO$_2$ and Ho@MSCeO$_2$ nanoparticles have the capability of scavenging free radicals by the exchange of Ce^{3+} and Ce^{4+} redox states constantly.[51,52] The XPS data also confirmed the existence of Ce^{3+}. This is the fundamental basis for the enhanced antibacterial behavior. It has also been reported that the contact of these nanoparticles with the bacterial membrane[7] can induce oxidative stress on the membrane through ROS production.[48,53]

The ROS species caused great destruction in bacteria through chemical degradation comprising DNA, proteins, and RNA.[54] Besides, Li et al.[55] studied that only the O$_2^{\bullet-}$ species were produced among other ROS species (i.e., $^\bullet$OH, O$_2$, and O$_2^{\bullet-}$) by CeO$_2$ nanoparticles upon UV irradiation. However, in this research, the antibacterial performances and production of O$_2^{\bullet-}$ and $^\bullet$OH were directed without UV irradiation. The EPR test in MS-CeO$_2$ nanoparticles (Figure 8a) revealed the successful detection of O$_2^{\bullet-}$, defect sites, the presence of Ce^{3+} and O vacancies under methanol solution, as well as $^\bullet$OH in DMPO (5,5-dimethyl-1-pyrroline N-oxide) at room temperature in Ho@MSCeO$_2$ nanoparticles[56] (Figure 8b). The four characteristic peaks of the quartet pattern of DMPO-$^\bullet$OH species were clearly detected and confirmed the production of $^\bullet$OH radicals in the sample (Figure 8b). On the contrary, for Ho@MSCeO$_2$ nanoparticles, a charge imbalance occurred by incorporating Ho^{3+} ions into CeO$_2$ nanoparticles to replace Ce^{4+} ions, generating the oxygen vacancy (O$_v$) defects while maintaining the integrity of the structure.[57] The role of

element partitioning was also studied by Sahoo et al.[58] with a europium dopant in the CeO$_2$ system, which promotes oxygen vacancies in the CeO$_2$ crystal.[58] The kinetic test via spectroscopic measurements (oxidation of a substrate) was also performed to further validate the ROS species (Figure S2).

Similarly, to analyze the phase, structure, crystallinity, and molecular interactions of MS-CeO$_2$ and Ho@MSCeO$_2$ nanoparticles, Raman spectroscopy was also performed (Figure 9). The main dominant peak of the Raman spectra located at
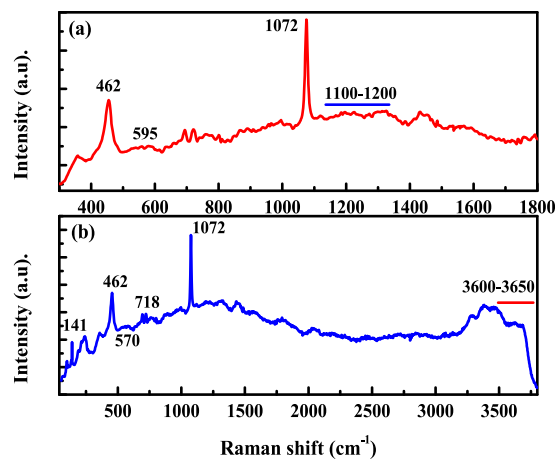
Figure 9. Raman spectra of MS-CeO$_2$ (a) and Ho@MSCeO$_2$ (b).

462 cm^{-1} is assigned to the fluorite phase of CeO$_2$, which is directed to the F$_{2g}$ mode, i.e., the stretching vibration of Ce—O$_8$ units,[59,60] while another peak at 1072 cm^{-1} is attributable to the typical second-order phonon mode of the cubic fluorite surface[60] (Figure 9a). The electronic structure of this phase is also different, i.e., residual electrons occupied the Ce f orbitals (presence of Ce^{3+} cations).[61] The curve band at 595 cm^{-1} observed in nanocrystallites is often called "the D-bands" (D as Defects) according to the Weber's study.[59,61] Such defect modes might be Frenkel-type oxygen defects present in crystalline nano CeO$_2$,[62,63] in which an oxygen atom at a lattice position is displaced to an interstitial site. While the peak ranges from 1100 to 1200 cm^{-1} implied that the oxygen vacancies are generated.[61] Moreover, the effects of the trivalent dopant in crystalline ceria were also studied by Raman spectroscopy and the following changes were examined, i.e., the F$_{2g}$ band at 464 cm^{-1} and the defect-induced mode at ∼570 cm^{-1} in the doped system case, as shown in Figure 9b.[64]

The bands from 3600 to 3650 cm^{-1} (Figure 9b) were ascribed to the OH$^-$ groups.[61] Figure 9b also describe the comparative intensity of the Eg mode at 141 cm^{-1} as the dopant amount. It indicated that dopant Ho affected the change from MS-CeO$_2$ to Ho@MSCeO$_2$, according to the XRD data.[65] Another broad peak at 718 cm^{-1} corresponded to the asymmetric broadening vibration of the Ce—O—Ce chains in metal oxide systems.[66]

3.4. Antibacterial Activity. The antibacterial activity of the synthesized pure MS-CeO$_2$ and Ho@MS-CeO$_2$ nanostructures was examined against two different distinctive bactericides, i.e., *E. coli* and *S. aureus.* which are as follows:

3.4.1. Antibacterial Activity of MS-CeO$_2$ Nanoparticles. Figure 10 presents the laden disk of *E. coli* and *S. aureus* suspensions of pure melon seed–like CeO$_2$ nanoparticles at (0.5, 1, and 2 mg/L) concentrations as well as the control group sample (1 mL of distilled water and 0.1% DMSO).
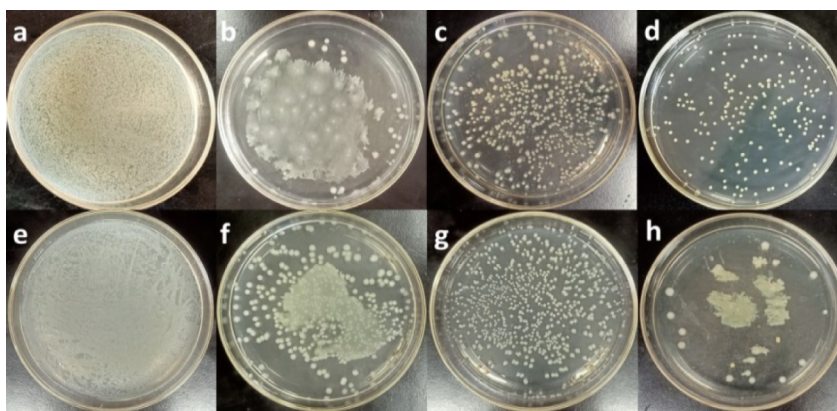
Figure 10. Photographs of *E. coli* and *S. aureus* mixture on MS-CeO$_2$ and control group after incubation at 37 °C for 24 h of antibacterial activity. (a, e) Control groups (1 L of distilled water and 0.1% DMSO) for *E. coli* and *S. aureus* mixture, (b) 0.5 mg/L CeO$_2$, (c) 1 mg/L CeO$_2$, and (d) 2 mg/L CeO$_2$ for *E. coli*, (f) 0.5 mg/L CeO$_2$, (g) 1 mg/L CeO$_2$, and (h) 2 mg/L CeO$_2$ for *S. aureus*.
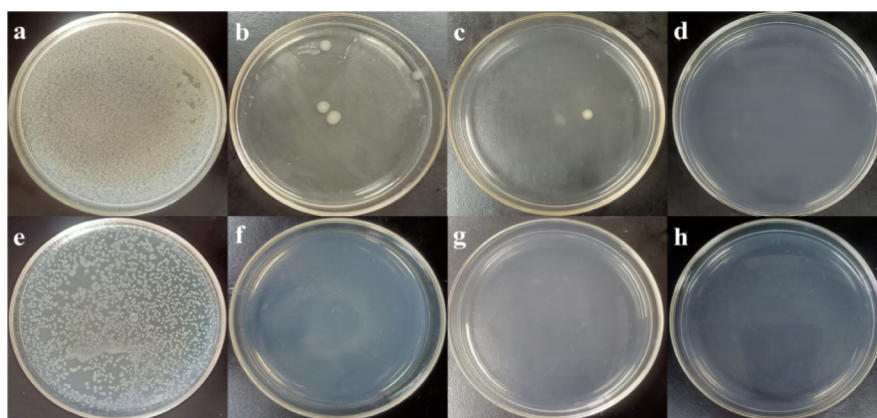

Figure 11. Photographs of *E. coli* mixtures on 1 and 3 wt % of Ho@MS-CeO$_2$ and control groups. (a, e) Control groups with 1 L of distilled water: (b) 0.5 mg/L (1 wt % Ho), (c) 1 mg/L (1 wt % Ho), (d) 2 mg/L (1 wt % Ho), (f) 0.5 mg/L (3 wt % Ho), (g) 1 mg/L (3 wt % Ho), and (h) 2 mg/L (3 wt % Ho).

Figure 12. Photographs of *S. aureus* mixtures with 1 and 3 wt % of Ho@MS-CeO$_2$ and control groups. (a, e) Control groups with 1 L of distilled water: (b) 0.5 mg/L (1 wt % Ho), (c) 1 mg/L (1 wt % Ho), (d) 2 mg/L (1 wt % Ho), (f) 0.5 mg/L (3 wt % Ho), (g) 1 mg/L (3 wt % Ho), and (h) 2 mg/L (3 wt % Ho).
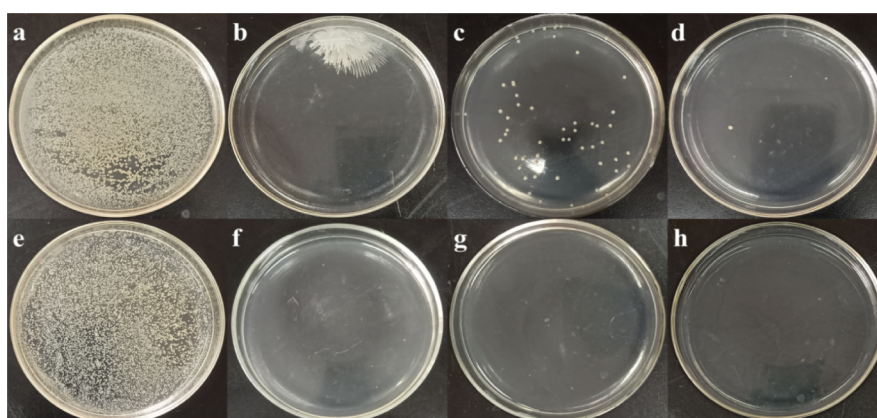
Control groups in the presence of *E. coli* and *S. aureus* samples contain numerous bacteria (Figure 10a,e) while *E. coli* and *S. aureus* numbers present on MS-CeO$_2$ nanoparticles decreased as the concentration changed from 0.5 mg/L to 2 mg/L (Figure 10b−d,f−h). Based on these data, it can be determined that the MS-CeO$_2$ nanoparticles have somehow exhibited

antibacterial properties as compared to the control group, which did not show any antibacterial effect.

In general, the antibacterial properties of ceria are governed by surface area, structure, morphology, surface charge, and oxygen vacancies, which permit the conversion of Ce^{4+} into Ce^{3+} ions and motivate ROS formation, as mentioned in the above XPS and EPR data in Figures 7 and 9.[67]
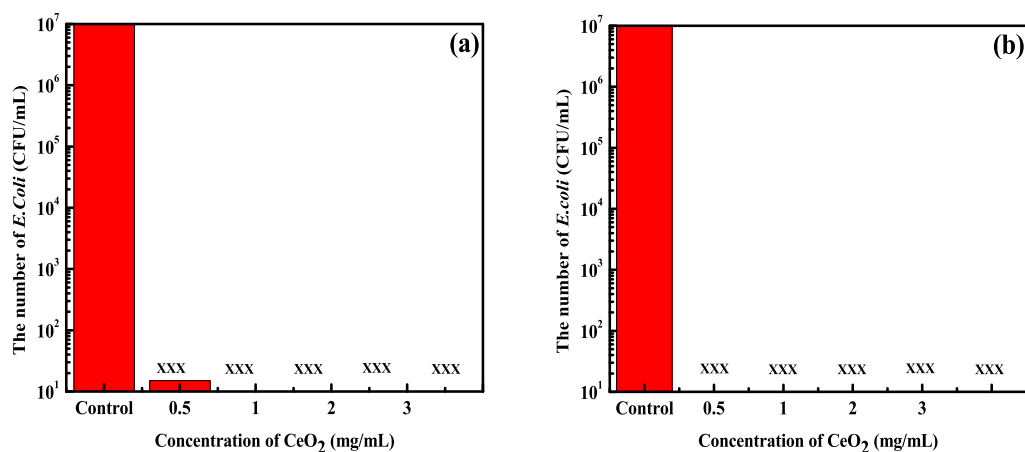
Figure 13. Algebraic data of colony number for *E. coli* suspensions:: (a) 1 wt % and (b) 3 wt % of Ho@MS-CeO$_2$ from 0.5 to 3 mg/L after incubation.

3.4.2. Antibacterial Activity of Ho@MS-CeO$_2$ Nanoparticles. Similar to pure MS-CeO$_2$, the Ho@MS-CeO$_2$ NPs were also subjected to the same concentrations (0.5, 1, and 2 mg/L) against both bacterial samples to check and compare their antibacterial activities. As shown in Figures 11 and 12, when the concentration of Ho was increased from 1 to 3 wt %, the toxicity of Ho@MS-CeO$_2$ NPs to both *E. coli* and *S. aureus* was increased. It was assumed that electrostatic interactions that occurred between (+) charged Ho@MS-CeO$_2$ nanoparticles and (−) charged bacteria were superior compared to pure MS-CeO$_2$ nanoparticles, leading to cell damage.[4] Therefore, the antibacterial property of Ho@MS-CeO$_2$ generated an enhanced rate from 0.5 to 2 mg/L.[4] The existence of trivalent ions (Ho^{3+}) is the main reason to generate the oxygen vacancies dependent on stoichiometry.[68,69] From comparison, it was noticed that Ho@MS-CeO$_2$ exhibited an excellent antimicrobial property against both bacterial samples (Figures 11 and 12).

Bacterial growth was also evaluated by assessing the number of colonies. This test showed that the antibacterial efficacy of pure MS-CeO$_2$ is nearly 40−50% at maximum concentration, i.e., 2 mg/L for both strains. However, 1 wt % Ho-doped MS-CeO$_2$ showed an excellent antibacterial activity at the same concentration (2 mg/L) for both bacterial suspensions. Moreover, 3 wt % Ho-doped MS-CeO$_2$ exhibited remarkable antibacterial activity at low concentrations (0.5 mg/L). Therefore, we assessed the colony numbers of 1 and 3 wt % of Ho@MS-CeO$_2$ in the *E. coli* strain (Figure 13). However, Ho@MS-CeO$_2$ showed a 100% response with *E. coli* at 3 wt % but an 80−90% response with *S. aureus* at 3 wt % concentration because of differences in bacterial strains. The effect of excessive Ho doping on the CeO$_2$ (Ho@MSCeO$_2$) nanoparticles was also evaluated (Figure S3).

3.4.3. Differences in Bacterial Strains. The as-prepared pure MS-CeO$_2$ and Ho@MS-CeO$_2$ nanostructures showed significant antibacterial effects against *E. coli* at different concentrations compared with *S. aureus*. The appearance of the microorganism membrane, its structure, surface charge, and metabolic action are closely related to the outer environment, which causes differences in antibacterial action.[70] Pelletier et al.[71] inspected the toxicity of the CeO$_2$ nanoparticles against *S. oneidensis*, *B. subtilis,* and *E. coli*. The results showed good antimicrobial efficiency against *B. subtilis* and *E. coli*, while no major inhibition was detected against *S. oneidensis* due to the

spore's effects. Therefore, MS-CeO$_2$ and Ho@MS-CeO$_2$ nanostructures showed similar results as those reported for different strains.[72] Moreover, the *S. aureus* cell wall mainly possessed a thick layer of peptidoglycan, which was cross-linked from side to side by small peptides to form an additional rigid structure. Thus, it was relatively difficult for any nanomaterial to easily contact or penetrate into *S. aureus* bacteria, while in (G$^-$) bacteria, the cell wall has a thinner peptidoglycan coating.[4]

3.4.4. Dilution Process of Ho@MS-CeO$_2$ Nanoparticles. Figure 14 shows the *E. coli* suspensions containing the disk of
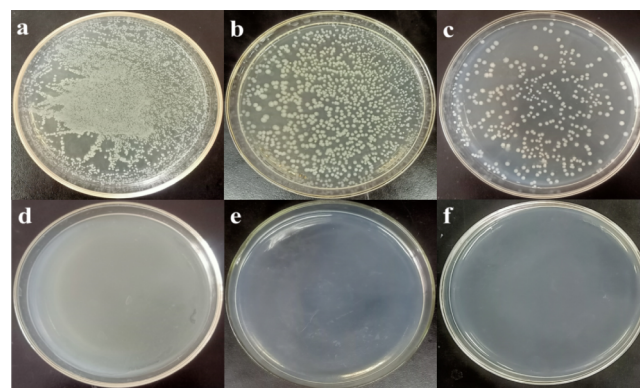

Figure 14. Photographs of *E. coli* suspensions of Ho@MS-CeO$_2$ nanoparticles versus control group samples. (a−c) Control groups with 1 L of distilled water at ×^{10},×^{100}, and ×^{1000} , while (d) 0.5 mg/L (X^{10}), (e) 0.5 mg/L (X^{100}), and (f) 0.5 mg/L (X^{1000}).

Ho@MS-CeO$_2$ (3 wt % Ho) NPs at a lower concentration (0.5 mg/L) as well as the control group (distilled water) samples in further diluted form to check the antibacterial activity. It can be seen that the standard control group samples have numerous bacteria existing, as revealed in Figure 14a−c, while no *E. coli* is present on the sample when the concentration of Ho@MS-CeO$_2$ is 0.5 mg/L (Figure 14d−f). These samples were diluted to approximately ×^{10}, ×^{100}, and ×^{1000} by adding 1 L of NaCl solution to them and examined to find that no bacteria were found in these samples, which indicated noteworthy antibacterial properties at very low concentrations too. The experimental data indicated that Ho@MS-CeO$_2$ nanostructures have impressive growth inhibitory effects on both types of bacteria and could be applied in several
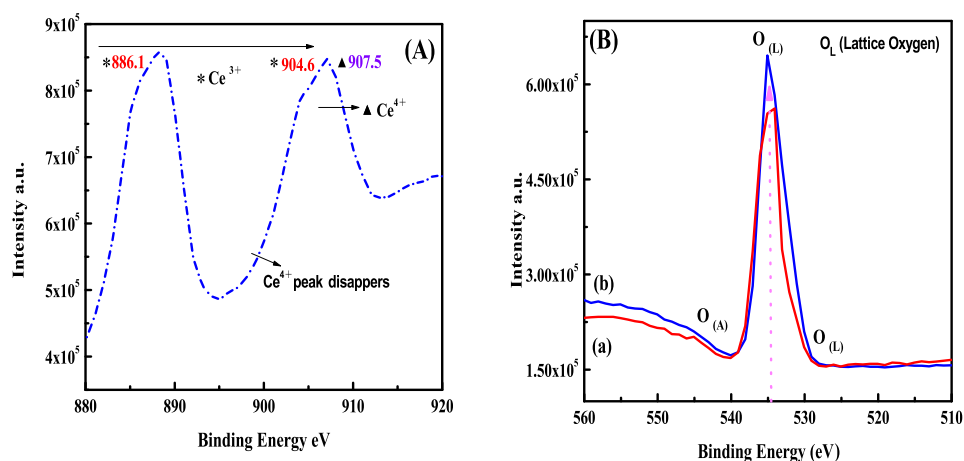
Figure 15. (A) XPS spectrum of Ho@MS-CeO$_2$ after antibacterial testing, which clearly shows the conversion of ions (Ce^{4+} reduced into Ce^{3+}), and (B) O 1s graph of O$_2$ peak intensities from XPS data, i.e. (a) MS-CeO$_2$ and (b) Ho@MS-CeO$_2$ peak intensities.

medical and antimicrobial regulatory systems.[67] These are fatal enough to counter the proteins and bind their molecules, repress cellular metabolism, and finally cause death of microbes.[67] Similarly, the same dilution process was performed with Ho@MS-CeO$_2$ at the same concentration of 0.5 mg/L, and it was found that similar remarkable results were obtained with *S. aureus* bacterial strains against the control group (Figure S4).

3.5. Mechanism Analysis of Antibacterial Properties. The supposed mechanism for the bactericidal effect of ceria nanomaterials is that they inactivate the cell's proteins after contact, and pierce inside bacteria, disable enzymes, and finally, cause death.[67,73] However in this case, they might interact directly to cell or produce secondary products that cause destruction.[53,69] Pulido-Reyes et al.[51] confirmed that the comparative percentage of Ce^{3+} to Ce^{4+} ions on the nanomaterial lattice surfaces significantly affected cellular toxicity. Hence, the prominent reasons for the excellent antibacterial activity can be understood in the following two aspects.

3.5.1. Conversion or Availability of Ce^{4+} and Ce^{3+}. It has been reported that the mixed valence states in ceria structures or the reversible conversion of Ce^{3+} and Ce^{4+} states has strongly been linked to the antioxidant properties of cerium-based systems.[74] For the claimed antimicrobial activity of Ho@MS-CeO$_2$ nanostructures, continuous reversible switching occurred on the ceria surface, which is a distinct property of CeO$_2$ lattices.[74] Figure 15A shows the XPS spectrum of Ho@MS-CeO$_2$ after the antibacterial test, which clearly shows the conversion of ions (Ce^{4+} reduced into Ce^{3+}). Figure 15B shows that the oxygen peak intensities of Ho@MS-CeO$_2$ have a higher peak intensity (O$_L$), which evidently specified the presence of more oxygen vacancies. The band energy was accredited to oxygen vacancies as well as usually attributed to weakly absorbed oxygen (O$_A$) on Ho@MS-CeO$_2$ nanoparticle surface, which in turn was associated with the Ce^{3+} ions.[75]

These holes dissociate H$_2$O molecules, and the dissolved oxygen is converted into anions that react with (H$^+$) ion to produce hydrogen peroxide (H$_2$O$_2$). The generated H$_2$O$_2$ can enter the cell membrane and might lead to the outflow of proteins, genetic materials, and minerals directly, which eventually causes cell death.[42,71,72] This type of mechanism does not need any contact between the microorganism and the bactericide. Second, the decrease in nanocrystalline size is

directly related to the increase in Ce^{3+} availability on the surfaces as the XPS data showed the high peak intensity of oxygen in Ho@MS-CeO$_2$ nanoparticles, which improved this property in some cases.[74] Therefore, the conversion of ions, size, and surface area are the key factors for the remarkable antibacterial properties of these nanomaterials.[71] Kuang et al.[76] also reported that the nanosized CeO$_2$ has better antibacterial effect as compared to the bulk CeO$_2$.

3.5.2. Zeta Potential. To explain the mechanism of the antibacterial properties of the doped nanostructure, the surface charge of the Ho@MS-CeO$_2$ sample was measured through the zeta potential technique. The synthesized Ho@MS-CeO$_2$ nanoparticles showed a positive potential of +4.06 mV (Figure 16).
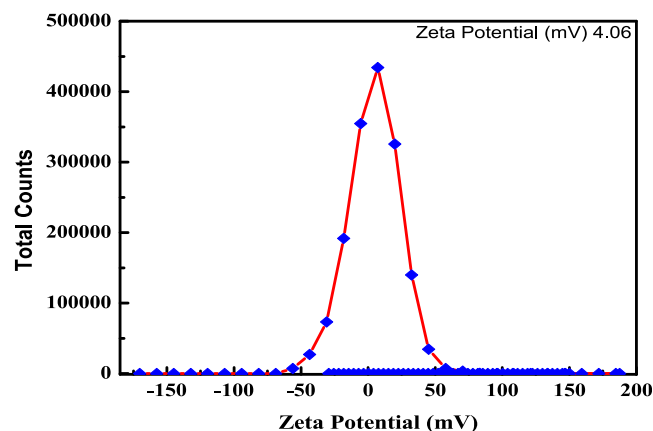

Figure 16. Zeta potential of Ho@MS-CeO$_2$ nanoparticles.

Notably, ceria nanomaterials synthesized with different kinds of surfactants yielded differently charged NPs.[54] Here, the positively charged Ho@MS-CeO$_2$ nanoparticles were promptly adsorbed on the membrane of negatively charged bactericides due to electrostatic attraction. Therefore, the positively charged Ho@MS-CeO$_2$ can damage the bacterial cell membrane.[42] For example, Zajac et al.[77] claimed that the nanoparticles were attached to the negatively charged bacterial cell membrane and shifted their electrical positive charge, leading to a reduction of bacterial growth. Nangia et al.[78] studied the surface-charge effects of nanoparticles on

negatively charged bacterial cell membranes. As predictable, the functionalization of nanoparticles with negatively charged surfaces was electrostatically resisted from the cell membrane, while positively charged or neutral nanoparticles interacted with the bacterial cell membrane. Furthermore, positively charged nanoparticles have played an important role in translocation processes. Zhang et al.[79] also explored the role of the charges of nanoparticles in attracting the bacterial membrane. The results showed that the γ-Fe_2O_3 nanoparticles with negative charges rarely interacted with the cell membrane while the positively charged Fe_2O_3 nanoparticles adhered to and penetrated in the membrane, disrupting even the overall negatively charged bacterial membrane. Furthermore, Mendes et al.[80] also checked the antibacterial activity and mechanism of ZnO nanoparticles against various bacterial strains. They found that electrostatic forces, Zn^{2+} ions, and ROS generation were defined as potential ways of antibacterial action of ZnO. On the contrary, it has a positive charge, with +24.0 mV zeta potential value. Accordingly, damage to the cell membrane occurred through the electrostatic gradient alterations between Zn^{2+} ions and the negatively charged membrane.

Hence, from the above discussion it is confirmed that the conversion of Ce^{4+} and Ce^{3+} ions, doping, and surface charge have a great effect on the excellent antibacterial properties of Ho@MS-CeO_2 nanoparticles. One of the most important properties is reversible conversion of Ce^{4+} and Ce^{3+} ions, which is directly related to the generation and migration of O vacancies.[7] Second, it was demonstrated that doping with Ho metal facilitated the generation of O vacancies and reduced Ce^{4+} into Ce^{3+}, resulting in significantly increasing the concentration of Ce^{3+} in the sample. Besides, the surface charge is also important to produce electrostatic interactions between nanomaterials and bacteria, causing damage to bacterial cell membranes.[42]

4. CONCLUSIONS

The pure CeO_2 (MS-CeO_2) and Ho-doped MS-CeO_2 (Ho@MS-CeO_2) nanoparticles with melon seed morphology were successfully synthesized by a simple precipitation method without adding any surfactant or organic complexing agent. The results demonstrated that, under certain stirring and aging temperatures, CeO_2 nanoparticles with melon seed−like morphology can be prepared in a short period. The MS-CeO_2 nanoparticles have an FCC crystal structure, with the crystallite size of approximately 13.1 nm with no phase impurities. The average crystallite size decreased after doping ceria with Ho, but the doping did not change the morphology. The antibacterial test results suggested that Ho@MS-CeO_2 has shown a remarkable antibacterial effect at low concentrations. The conversion of Ce^{4+} and Ce^{3+} ions, doping, and surface charge may play important roles in enhancing the antibacterial activity. Overall, the Ho@MS-CeO_2 nanostructures showed a tremendous antibacterial response due to the presence of more oxygen vacancies. This study suggested that synthesized pure and doped CeO_2 nanomaterials through this method have potential applications in biomedical and food storage industries.

ASSOCIATED CONTENT

Ⓢ Supporting Information

The Supporting Information is available free of charge at https://pubs.acs.org/doi/10.1021/acsomega.4c01112.

The data of different stirring times were displayed through SEM images; the average crystallite sizes of synthesized undoped and doped MS-CeO_2 nanoparticles were calculated through XRD; the wavenumber's location and vibrational modes of several adsorbed chemical groups on the surface were evaluated through FTIR spectrum as well as the attribution of cerium peaks observed in XPS spectra was expressed in table form. Furthermore, the dilution process data of antibacterial activity of Ho@MS-CeO_2 nanostructures for *S. aureus* were also mentioned through images (PDF)

AUTHOR INFORMATION

Corresponding Author

Xue Li − *School of Chemistry and Chemical Engineering, University of Jinan, Jinan 250022, PR China;* ⊙ orcid.org/0000-0002-9018-7029; Email: chm_lix@ujn.edu.cn

Authors

Kanwal Javed − *School of Chemistry and Chemical Engineering, University of Jinan, Jinan 250022, PR China*

Yufang Ren − *School of Chemistry and Chemical Engineering, University of Jinan, Jinan 250022, PR China*

Zhenhao Cao − *School of Chemistry and Chemical Engineering, University of Jinan, Jinan 250022, PR China*

Bushra Begum − *Department of NCEPC, University of Peshawar, Peshawar, Khyber Pakhtunkhwa 25120, PR Pakistan*

Yifan Liu − *School of Chemistry and Chemical Engineering, University of Jinan, Jinan 250022, PR China*

Aamad Ullah Zafar − *Department of Chemical Engineering, University of Engineering and Technology, University of Peshawar, Peshawar, Khyber Pakhtunkhwa 25120, PR Pakistan*

Complete contact information is available at:
https://pubs.acs.org/10.1021/acsomega.4c01112

Notes

The authors declare no competing financial interest.

REFERENCES

(1) Ates, T. Synthesis and characterization of Ag-doped CeO_2 powders. *J. Aust. Ceram. Soc.* 2021, 57, 615−623.

(2) Majumder, D.; Chakraborty, I.; Mandal, K. Room temperature blooming of CeO_2 3D nanoflowers under sonication and catalytic efficacy towards CO conversion. *RSC Adv.* 2020, 10, 22204−22215.

(3) Jiang, W.; Loh, H.; Low, B. Q. L.; Zhu, H.; Low, J.; Heng, J. Z. X.; Tang, K. Y.; Li, Z.; Loh, X. J.; Ye, E.; Xiong, Y. Role of oxygen vacancy in metal oxides for photocatalytic CO_2 reduction. *Appl. Catal., B* 2023, 321, 122079.

(4) Khader, Y. A. S.; Balamurugan, A.; Devarajan, V. P.; Subramanian, R.; Kumar, S. D. Synthesis, characterization and antibacterial activity of cobalt doped cerium oxide (CeO_2: Co) nanoparticles by using hydrothermal method. *J. Mater. Res. Technol.* 2019, 8, 267−274.

(5) Govindarasu, K.; Gnanasekaran, K.; Balaraman, S.; Iruson, B.; Krishnamoorthy, S.; Balaraman, S.; Padmaraj, B.; Manikandan, E.; Dhananjayan, S. Study on enhanced antibacterial cytotoxicity of pure and cadmium doped cerium oxide against gram-positive and gram-negative bacteria. *Soft Nanosci. Lett.* 2019, 9 (01), 1−16.

(6) Qi, M.; Li, W.; Zheng, X.; Li, X.; Sun, Y.; Wang, Y.; Li, C.; Wang, L. Cerium and its Oxidant-based nanomaterials for antibacterial applications: A state-of-the-art review. *Front. Mater. Sci.* **2020**, 7, 213.

(7) Nadeem, M.; Khan, R.; Afridi, K.; Nadhman, A.; Ullah, S.; Faisal, S.; Mabood, Z. U.; Hano, C.; Abbasi, B. H. Green synthesis of cerium oxide nanoparticles (CeO_2 NPs) and their antimicrobial applications: A Review. *Int. J. Nanomed.* **2020**, 15, 5951−5961.

(8) Khader, Y. A. S.; Balamurugan, A.; Devarajan, V. P.; Subramanian, R. Hydrothermal synthesis of Gadolinium (Gd) doped cerium oxide (CeO_2) nanoparticles: characterization and antibacterial activity. *Orient. J. Chem.* **2017**, 33, 2405−24011.

(9) Balamurugan, A.; Sudha, M.; Surendhiran, S.; Anandarasu, R.; Ravikumar, S.; Khadar, Y. A. S. Hydrothermal synthesis of samarium (Sm) doped cerium oxide (CeO_2) nanoparticles: characterization and antibacterial activity. *Mater. Today* **2020**, 26, 3588−3594.

(10) Negi, K.; Umar, A.; Chauhan, M. S.; Akhtar, S. Ag/CeO2 nanostructured materials for enhanced photocatalytic and antibacterial applications. *Ceram. Int.* **2019**, 45, 20509−20517.

(11) Gnanam, S.; Gajendiran, J.; Ramya, J. R.; Ramachandran, K.; Raj, S. G. Glycine-assisted hydrothermal synthesis of pure and europium doped CeO2 nanoparticles and their structural, optical, photoluminescence, photocatalytic and antibacterial properties. *Chem. Phys. Lett.* **2021**, 763, 138217.

(12) Parimi, D.; Sundararajan, V.; Sadak, O.; Gunasekaran, S.; Mohideen, S. S.; Sundaramurthy, A. Synthesis of Positively and Negatively Charged CeO_2 Nanoparticles: Investigation of the Role of Surface Charge on Growth and Development of Drosophila melanogaster. *ACS Omega* **2019**, 4, 104−113.

(13) Sun, C.; Li, H.; Wang, Z. X.; Chen, L.; Huang, X. Synthesis and characterization of polycrystalline CeO_2 nanowires. *Chem. Lett.* **2004**, 33, 662−664.

(14) Cam, T. S.; Omarov, S. O.; Chebanenko, M. I.; Izotova, S. G.; Popkov, V. I. Recent progress in the synthesis of CeO_2-based nanocatalysts towards efficient oxidation of CO. *J. Advance. Mater.* **2022**, 7, 100399−100410.

(15) Rodriguez, J. A.; Grinter, D. C.; Liu, Z.; Palomino, R. M.; Senanayake, S. D. Ceria-based model catalysts: fundamental studies on the importance of the metal−ceria interface in CO oxidation, the water−gas shift, CO_2 hydrogenation, and methane and alcohol reforming. *Chem. Soc. Rev.* **2017**, 46 (7), 1824−1841.

(16) Fan, L.; Wang, C.; Chen, M.; Zhu, B. Recent development of ceria-based (nano) composite materials for low temperature ceramic fuel cells and electrolyte-free fuel cells. *J. Power Sources* **2013**, 234, 154−174.

(17) Sun, C.; Li, H.; Chen, L. Nanostructured ceria-based materials: synthesis, properties and applications. *Energy Environ. Sci.* **2012**, 5, 8475−8505.

(18) Kpenekci, O. Hydrothermal Preparation of single crystalline CeO_2 nanoparticles and the influence of alkali hydroxides on their structure and optical behavior 2009.

(19) Zulfiqar, M. Investigations on Gadolinium doped ceria electrolyte prepared via sol-gel and co-precipitation routes for intermediate temperature solid oxide fuel cell (ITSOFC) applications *4th International Conference on Energy, Environment and Sustainable Development (EESD)*; MUET, 2016.

(20) Hapsari, A. U.; Raharjo, J.; Yuliani, H.; Suradharmika, I. G. A.; Damisih; Pravitasari, R. D.; Sari, D. P. Synthesis and characterization of gadolinium doped cerium (Ce0,9Gd0,1O1,95) by using various carbonates as a precipitant. *IOP Conf. Ser. Mater. Sci. Eng.* **2019**, 622 (1), 012011.

(21) Gong, J.; Meng, F.; Yang, X.; Fan, Z.; Li, H. Controlled hydrothermal synthesis of triangular CeO_2 nanosheets and their formation mechanism and optical properties. *J. Alloys Compd.* **2016**, 689, 606−616.

(22) Xu, Y. *Morphological mapping and growth mechanisms of ceria nanocrystals* Master of Philosophy thesis; UNSW Sydney, Australia, 2019.

(23) Yang, K.; Rong, J.; Feng, J.; Zhuang, Y.; Zhao, H.; Wang, L.; Ni, J.; Tao, S.; Shao, F.; Ding, C. Excellent wear resistance of plasma-sprayed amorphous Al_2O_3-$Y_3Al_5O_{12}$ ceramic coating. *Surf. Coat. Technol.* **2017**, 326, 96−102.

(24) Balavandy, S. K.; Shameli, K.; Biak, D. R. B. A.; Abidin, Z. Z. Stirring time effect of silver nanoparticles prepared in glutathione mediated by green method. *Chem. Cent. J.* **2014**, 8 (1), 11.

(25) Sakthivel, T.; Das, S.; Kumar, A.; Reid, D.; Gupta, A.; Sayle, D.; Seal, S. Morphological phase diagram of bio-catalytically active ceria nanostructures as a function of processing variables and their properties. *Chem. Plus. Chem.* **2013**, 78, 1446−1455.

(26) Zhang, D.; Gu, J.; Xie, Q.; Li, S.; Zhang, X.; Han, G.; Ying, A.; Tong, Z.; Li, F. Controlled synthesis of $Ce(OH)CO_3$ flowers by a hydrothermal method and their thermal conversion to CeO_2 flowers. *Particuology* **2012**, 10, 771−776.

(27) Murugadoos, G.; Ma, J.; Ning, X.; Kumar, M. R. Selective metal ions doped CeO_2 nanoparticles for excellent photocatalytic activity under sunlight and supercapacitor application. *Inorg. Chem. Commun.* **2019**, 109, 107577.

(28) Jameel, M. S.; Aziz, A. A.; Dheyab, M. A. Green synthesis: Proposed mechanism and factors influencing the synthesis of platinum nanoparticles. *Green Process. Synth.* **2020**, 9, 386−398.

(29) Basri, H. H.; Talib, R. A.; Sukor, R.; Othman, S. H.; Ariffin, H. Effect of synthesis temperature on the size of ZnO nanoparticles derived from pine apple peel extract and antibacterial activity of ZnO-Starch nanocomposite films. *Nanomaterials* **2020**, 10, 1061.

(30) Wu, Q.; Zhang, F.; Xiao, P.; Tao, H.; Wang, X.; Hu, Z.; Lü, Y. Great Influence of Anions for controllable synthesis of CeO_2 Nanostructures: From nanorods to nanocubes. *J. Phys. Chem. C* **2008**, 112 (44), 17076−17080.

(31) Kashyap, K.; Khan, F.; Verma, D.; Agrawal, S.; Chandra, C.; Dewangan, P. K.; Sahu, V.; Verma, P. R.; Jain, V. K. Biofabrication and structural characterization of cerium oxide nanoparticles. *IOP Conf. Ser. Mater. Sci. Eng.* **2021**, 1120 (1), 012008.

(32) Liu, F.; Wang, Z.; Wang, D.; Chen, D.; Chen, F.; Li, X. Morphology and crystal-plane effects of Fe/W-CeO_2 for selective catalytic reduction of NO with NH_3. *Catalysts* **2019**, 9, 288.

(33) Tumkur, P. P.; Gunasekaran, N. K.; Lamani, B. R.; Bayon, N. N.; Prabhakaran, K.; Hall, J. C.; Ramesh, G. T. Cerium oxide nanoparticles: synthesis and characterization for biosafe applications. *Nanomanufacturing* **2021**, 1, 176−189.

(34) Wei, J.; Yang, Z.; Yang, H.; Sun, T.; Yang, Y. A mild solution strategy for the synthesis of mesoporous CeO_2 nanoflowers derived from $Ce(HCOO)_3$. *CrystEngComm.* **2011**, 13 (15), 4950−4956.

(35) Karem, I. K. A.; Hamdan, S. A. The influence of CeO_2 concentration of some physical properties of Y_2O_3 thin. *Iraqi J. Sci.* **2022**, 63, 2482−2491.

(36) Dwivedi, A.; Srivastava, M.; Srivastava, A.; Upadhyay, C.; Srivastava, S. K. Tunable photoluminescence and energy transfer of Eu^{3+}, Ho^{3+} doped $Ca_{0.05}Y_{1.93-x}O_2$ nanophosphors for warm white LEDs applications. *Sci. Rep.* **2022**, 12 (1), 5824−5839.

(37) Cheng, J.; Huang, S.; Li, Y.; Wang, T.; Xie, L.; Lu, X. RE (La, Nd and Yb) doped CeO2 abrasive particles for chemical mechanical polishing of dielectric materials: Experimental and computational analysis. *Appl. Surf. Sci.* **2020**, 506, 144668.

(38) Dagnall, K. A.; Conley, A. M.; Yoon, L. U.; Rajeev, S. F.; Lee, S. H.; Choi, J. J. Ytterbium-doped cesium lead chloride perovskite as an X-ray scintillator with high light yield. *ACS Omega* **2022**, 7, 20968−20974.

(39) Zhao, R.; Huan, L.; Gu, P.; Guo, R.; Chen, M.; Diao, G. Yb, Er-doped CeO_2 nanotubes as an assistant layer for photo-conversion-enhanced dye-sensitized solar cells. *J. Power Sources* **2016**, 331, 527−534.

(40) Ayon, S. A.; Billah, M. M.; Nishat, S. S.; Kabir, A. Enhanced photocatalytic activity of Ho^{3+} doped ZnO NPs synthesized by modified sol-gel method: An experimental and theoretical investigation. *J. Alloys Compd.* **2021**, 856, 158217−158232.

(41) Han, T.; Ma, S.; Yun, P.; Sheng, H.; Xu, X.; Cao, P.; Pei, S.; Alhadi, A. Synthesis and characterization of Ho-doped $SmFeO_3$ nanofibers with enhanced glycol sensing properties. *Vaccum* **2021**, 191, 110378−110383.

(42) Parvathya, S.; Venkatramanb, B. R. Invitro antibacterial and anticancer potential of CeO_2 nanoparticles prepared by co-precipitation and green synthesis method. *J. Nanosci. Curr. Res.* **2017**, *2* (2), 111.

(43) Li, Y.; Li, Y.; Wang, H.; Liu, R. Yb^{3+}, Er^{3+} Co-doped cerium oxide up conversion nanoparticles enhanced the enzyme like catalytic activity and anti-oxidative activity for parkinson's disease treatment. *ACS Appl. Mater.* **2021**, *13*, 13968−13977.

(44) Seminko, V.; Maksimchuk, P.; Klochkov, V.; Yefimova, S. Luminescent colloidal ceria nanoparticles doped with RE^{3+} ions (RE = Eu, Tb) via cation exchange mechanism. *J. Lumin.* **2022**, *242*, 118605.

(45) Liu, L.; Shi, J.; Cao, H.; Wang, R.; Liu, Z. Fabrication of CeO_2-MO_X (M = Cu, Co, Ni) composite yolk-shell nanospheres with enhanced catalytic properties for CO oxidation. *J. Nanotechnol.* **2017**, *8*, 2425−2437.

(46) Lee, H. I.; Lee, S. W.; Rhee, C. K.; Sohn, Y. Paramagnetic Ho_2O_3nanowires, nano-square sheets, and nanoplates. *Ceram. Int.* **2018**, *4*, 17919−17924.

(47) Clabel H, J. L.; Lozano, G.; Marega, E., Jr; Rivera, V. A. G. XPS analysis of bridging and non-bridging oxygen in Yb, Er, Tm- doped zinc-tellurite glasses. *J. Non-Cryst. Solids* **2021**, *553*, 120520.

(48) Zhang, M.; Zhang, C.; Zhai, X.; Luo, F.; Du, Y.; Yan, C. Antibacterial mechanism and activity of cerium oxide nanoparticles. *Sci. China Mater.* **2019**, *62*, 1727−1739.

(49) Maslakov, K. I.; Teterin, Y. A.; Popel, A. J.; Teterin, A. Y.; Ivanov, K. E.; Kalmykov, S. N.; Petrov, V. G.; Petrov, P. K.; Farnan, I. XPS study of ion irradiated and unirradiated CeO_2 bulk and thin film samples. *Appl. Surf. Sci.* **2018**, *448*, 154−162.

(50) Sadidi, H.; Hooshmand, S.; Ahmadabadi, A.; Hoseini, S. J.; Baino, F.; Vatanpour, M.; Kargozar, S. Cerium oxide nanoparticles (nanoceria): Hopes in soft tissue engineering. *Molecules* **2020**, *25* (19), 4559.

(51) Pulido-Reyes, G.; Rodea-Palomares, I.; Das, S.; Sakthivel, T. S.; Leganes, F.; Rosal, R.; Seal, S.; Fernández-Piñas, F. Untangling the biological effects of cerium oxide nanoparticles: The role of surface valence states. *Sci. Rep.* **2015**, *5*, 15613.

(52) Celardo, I.; Pedersen, J. Z.; Traversa, E.; Ghibelli, L. Pharmacological potential of cerium oxide nanoparticles. *Nanoscale* **2011**, *3*, 1411−1420.

(53) Thill, A.; Zeyons, O.; Spalla, O.; Chauvat, F.; Rose, J.; Auffan, M.; Flank, A. M. Cytotoxicity of CeO_2 nanoparticles, physico-chemical insight of the cytotoxicity mechanism. *Environ. Sci. Technol.* **2006**, *40*, 6151−6156.

(54) Aruguete, D. M.; Kim, B.; Hochella, M. F., Jr; Ma, Y.; Cheng, Y.; Hoegh, A.; Liu, J.; Pruden, A. Antimicrobial nanotechnology: Its potential for the effective management of microbial drug resistance and implications for research needs in microbial nano-toxicology. *Environ. Sci. Proc. Imp.* **2013**, *15*, 93−102.

(55) Li, Y.; Zhang, W.; Niu, J.; Chen, Y. Mechanism of photo-generated reactive oxygen species and correlation with the antibacterial properties of engineered metal-oxide nanoparticles. *ACS Nano* **2012**, *6* (6), 5164−5173.

(56) Xiao, J.; Yang, X.; Zhao, X.; Qin, F.; Yang, X.; Cui, L.; Zhou, Z.; Lin, D.; Hu, Z.; Qin, Y.; Zhang, J. Synergy between platinum and oxygen vacancy in CeO_2 boosting enzyme-mimicking activity. *Biochem. Eng. J.* **2024**, *202*, 109165−109173.

(57) Colis, S.; Bouaine, A.; Schmerber, G.; Ulhaq-Bouillet, C.; Dinia, A.; Choua, S.; Turek, P. High-temperature ferromagnetism in Co-doped CeO_2 synthesized by the co-precipitation technique. *Phys. Chem. Chem. Phys.* **2012**, *14*, 7256−7263.

(58) Sahoo, S. K.; Mohapatra, M.; Anand, S. Characterization and optical properties of Eu-doped cubic nano ceria synthesized by using the co-precipitation-hydrothermal route. *J. Korean Phys. Soc.* **2013**, *62*, 297−304.

(59) Bai, J. Q.; Lv, L.; Liu, J.; Wang, Q.; Cheng, Q.; Cai, M.; Sun, S. Control of CeO_2 defects sites for photo-and thermal-synergistic catalysis of CO_2 and methanol to DMC. *Catal. Lett.* **2023**, *153*, 3209−3218.

(60) Choi, Y. M.; Abernathy, H.; Chen, H. T.; Lin, M. C.; Liu, M. Characterization of O_2-CeO_2 interactions using in situ Raman spectroscopy and first-principle calculations. *ChemPhyschem* **2006**, *7*, 1957−1963.

(61) Loridant, S. Raman spectroscopy as a powerful tool to characterize ceria-based catalysts. *Catal. Today* **2021**, *373*, 98−111.

(62) Wu, Z.; Li, M.; Howe, J.; Meyer, H. M.; Overbury, S. H. Probing defect sites on CeO_2 nanocrystals with well-defined surface Planes by Raman spectroscopy and O_2 adsorption. *Langmuir* **2010**, *26*, 16595−16606.

(63) Agarwal, S.; Zhu, X.; Hensen, E. J. M.; Mojet, B. L.; Lefferts, L. Surface-dependence of defect chemistry of nanostructured Ceria. *J. Phys. Chem. C* **2015**, *119*, 12423−12433.

(64) Schilling, C.; Hofmann, A.; Hess, C.; Pirovano, M. V. G. Raman spectra of polycrystalline CeO_2: A density functional theory study. *J. Phys. Chem. C* **2017**, *121* (38), 20834−20849.

(65) Liu, X.; Fang, P.; Liu, Y.; Liu, Z.; Lu, D.; Gao, Y.; Chen, F.; Wang, D.; Dai, Y. Effect of holmium doping on the structure and the photocatalytic behavior of TiO_2-based nanosheets. *J. Mater. Sci* **2014**, *49*, 8063−8073.

(66) Ankita, A.; Chahal, S.; Singh, S.; Kumar, S.; Kumar, P. Europium-doped cerium oxide nanoparticles: investigating oxygen vacancies and their role in enhanced photocatalytic and magnetic properties. *Environ. Sci. Pollut. Res.* **2024**, *31*, 1276−1287.

(67) Kannan, S. K.; Sundrarajan, M. A Green Approach for the Synthesis of a Cerium Oxide Nanoparticle: Characterization and Antibacterial Activity. *Int. J. Nanosci.* **2014**, *13* (03), 1450018.

(68) Sun, Q.; Fu, Z.; Yang, Z. Effects of rare-earth doping on the ionic conduction of CeO_2 in solid oxide fuel cells. *Ceram. Int.* **2011**, *44*, 3707−3711.

(69) Shehata, N.; Meehan, K.; Hudait, M.; Jain, N.; Gaballah, S. Study of optical and structural characteristics of ceria nanoparticles doped with negative and positive association lanthanide elements. *J. Nanomater.* **2014**, *2014*, 156−163.

(70) Yadav, S. L. R.; Manjunath, K.; Archana, B.; Madhu, C.; Naika, H. R.; Nagabbhushana, H.; Kavitha, C.; Nagaraju, G. Fruit juice extract mediated synthesis of CeO_2 nanoparticles for antibacterial and photocatalytic activities. *Eur. Phys. J. Plus* **2016**, *131*, 8.

(71) Pelletier, D. A.; Suresh, A. K.; Holton, G. A.; Mckeown, C. K.; Wang, W.; Gu, B.; Mortensen, N. P.; Allison, D. P.; Joy, D. C.; Allison, M. R.; Joy, D. C.; Allison, M. R.; Brown, S. D.; Phelps, T. J.; Doktycz, M. J. Effects of engineered cerium oxide nanoparticles on bacterial growth and viability. *Appl. Environ. Microbiol.* **2010**, *76*, 7981−7991.

(72) Surendra, T. V.; Roopan, S. M. Photocatalytic and antibacterial properties of phytosynthesized of CeO_2 NPs using *Moringa oleifera* peel extract. *J. Photochem. Photobiol., A* **2016**, *161*, 122−128.

(73) Staron, A.; Dluogosz, O. Antimicrobial properties of nano-particles in the context of advantages and potential risks of their use. *J. Environ. Sci. Health A* **2021**, *56*, 680−693.

(74) Bassous, N. J.; Garcia, C. B.; Webster, T. J. A study of the chemistries, growth mechanisms, and antibacterial properties of cerium- and yttrium-containing nanoparticles. *Biomater. Sci. Eng.* **2021**, *7*, 1787−1807.

(75) Kumar, K. M.; Mahendhiran, M.; Diaz, M. C.; Hernandez-Como, M.; Hernandez-Eligio, A.; Torres-Torres, G.; Godavarthi, S.; Gomez, L. M. Green synthesis of Ce^{3+} rich CeO_2 nanoparticles and its antimicrobial studies. *Mater. Lett.* **2018**, *214*, 15−19.

(76) Kuang, Y.; He, X.; Zhang, Z.; Li, Y.; Zhang, H.; Ma, Y.; Wu, Z.; Chai, Z. Comparison study on the antibacterial activity of nano- or bulk-cerium oxide. *J. Nanosci. Nanotechnol.* **2011**, *11*, 4103−4108.

(77) Zajac, M.; Kotynska, J.; Zambrowski, G.; Breczko, J.; Deptula, P.; Ciesluk, M.; Zambrzycka, M.; Swieccicka, I.; Bucki, R.; Naumowicz, M. Exposure to polystyrene nanoparticles leads to changes in the zeta potential of bacterial cells. *Sci. Rep.* **2023**, *13* (1), 9552−9568.

(78) Nangia, S.; Sureshkumar, R. Effects of nanoparticle charge and shape anisotropy on translocation through cell membranes. *Langmuir* **2012**, *28*, 17666−17671.

(79) Zhang, H.; Wei, X.; Liu, L.; Zhang, Q.; Jiang, W. The role of positively charged sites in the interaction between model cell membranes and γ-Fe$_2$O$_3$ NPs. *Sci. Total Environ.* **2019**, *673*, 414−423.

(80) Mendes, C. R.; Dilarri, G.; Forsan, C. F.; Sapata, V. D. M. R.; Lopes, P. R. M.; Moraes, P. B. D.; Montagnolli, R. N.; Ferreira, H.; Bidoia, E. D. Antibacterial action and target mechanisms of zinc oxide nanoparticles against bacterial pathogens. *Sci. Rep.* **2022**, *12* (1), 2658−2668.